

## Fluid-phase helium: Shock-compression experiments, quantum molecular dynamics simulations, and development of an equation of state

Philip C. Myint<sup>1,\*</sup>, Seth Root<sup>2,\*</sup>, Christine J. Wu<sup>1,\*</sup>, Raymond C. Clay<sup>2</sup>, Andrew Lopez<sup>2</sup>, Heath L. Hanshaw<sup>2</sup>, Raymond W. Lemke<sup>2</sup>, David E. Bliss<sup>2</sup>, David L. Hanson<sup>2</sup>, Dawn G. Flicker<sup>2</sup>, and Zoë C. Long<sup>1</sup>

<sup>1</sup>Lawrence Livermore National Laboratory, Livermore, California 94550, USA

<sup>2</sup>Sandia National Laboratories, Albuquerque, New Mexico 87185, USA



(Received 11 April 2023; revised 10 August 2023; accepted 25 September 2023; published 18 October 2023)

Helium (He) plays a critical role in numerous areas ranging from the study of celestial objects like brown dwarfs and gas giants to modern-day technologies like nuclear energy and rocket propulsion. For many of these applications, it is essential to have a reliable equation of state (EOS) for He that yields an accurate representation of its thermodynamic behavior. To help constrain and develop such EOS models, we have performed a series of shock-compression experiments on cryogenic liquid He to pressures exceeding 100 GPa using a magnetically accelerated flyer plate on Sandia National Laboratories' Z-machine. We have also performed quantum molecular dynamics simulations that are consistent with our shock measurements. None of the previously available EOSs agree with our experimental and simulation results, motivating the development of a fluid-phase He EOS that we present in this study. We show that our EOS yields good agreement with published data that span temperatures and pressures encountered across a diverse array of applications.

DOI: [10.1103/PhysRevB.108.134202](https://doi.org/10.1103/PhysRevB.108.134202)

### I. INTRODUCTION

As the second-most abundant element in the universe, the ubiquitous presence of helium (He) is apparent in many fields of study and applications. As an inert gas with an incredibly low melting point, it finds wide use in industrial applications as a benign working fluid and for cryogenics [1]. Since He is also produced in nuclear decay, it plays an important role in the aging of nuclear reactors, and multiple studies motivated by this application have examined the behavior of compressed He bubbles embedded in metals [2–7]. Under more extreme thermodynamic conditions, it is a major constituent of stars, brown dwarfs, Jovian planets, and other astrophysical bodies [8–10].

Modeling the behavior of He at macroscopically relevant scales for these applications requires equations of state (EOSs), which specifies thermodynamic properties (e.g., internal energy) as a function of temperature and density or pressure. Many of the available equations of state for He are domain specific. For EOSs targeting industrial applications, the wealth of experimental data at ambient or relatively close to ambient conditions (typically temperatures below 1000 K and pressures below 1 GPa) allows the construction of empirical multiparameter EOS models [1, 11–14]. Key properties that these multiparameter models try to reproduce are the critical point, which lies at around 5 K and 2 bar, and the vapor-liquid dome. In contrast, astrophysical EOS models are designed primarily for high temperature and pressure regimes where known asymptotic limits and simplified

models of atomic structure can produce accurate equations of state, though these models also attempt to describe ambient or near-ambient conditions where He exists as a dense supercritical fluid or a gas. The most well-known such model is that by Saumon, Chabrier, and van Horn, which is commonly referred to as the SCvH (or SCVH) EOS in the literature [8]. This model, as well as more recent ones by Chabrier *et al.* [10] and Becker *et al.* [9] that are based in part on SCvH, have shown considerable success in modeling Jovian planets and white dwarfs.

For inertial confinement fusion and dynamic materials experiments fielded at institutions such as Lawrence Livermore National Laboratory's National Ignition Facility [15, 16] and Sandia's Z-machine [17], domain-specific equations of state break down: the multiparameter models extrapolate past the limited range of data over which they were fit, and the astrophysical models typically end up having insufficient fidelity to capture the complicated material properties of cooler denser conditions. There is thus a strong motivation to construct equations of state that are capable of describing the properties of He from ambient conditions all the way to multimegabar conditions. Because of this wide range of conditions considered by such EOS models, which necessarily requires accounting for ionization and electronic excitations, they are typically represented in a tabular form (e.g., with pressure printed out over a grid of temperatures and densities), rather than closed-form, analytical expressions. One such EOS for He is the LEOS 20 table, which we henceforth refer to as L20, that was developed by Young *et al.* over 30 years ago [18–20]. Another example is the SESAME 5764 (S5764) table developed by Kerley [21], which is a two-phase (fluid-solid) EOS published back in 2004, more than a decade after the development of L20. Both of these models were fit to

\*These authors contributed equally to this work; corresponding authors: myint1@llnl.gov, sroot@sandia.gov, wu5@llnl.gov

experimental data available at the time, usually in the form of static-compression (diamond-anvil cell) data [22–26] at or near room temperature and limited dynamic-compression data [27]. While L20 and S5764 have their regimes of validity, recent experiments and *ab initio* calculations at higher temperatures and densities have exposed inaccuracies in both of these tables.

To this end, through a combined experimental, modeling, and theory effort, we have constructed a fluid-phase EOS, which we refer to as L21. We have performed strong shocks on He samples at cryogenic conditions using Sandia’s Z-machine, which reached pressures between 50 GPa and 125 GPa, the highest shock pressures attained on cryogenically cooled, liquid He. In addition, we have performed quantum molecular dynamics (QMD) simulations up to 250 GPa to complement our experiments. Building on our recent EOS work for other materials [28–30], we use these data in conjunction with existing experimental and *ab initio* data to constrain our L21 EOS model and demonstrate its performance. We divide the rest of this paper as follows. Section II describes our experiments, QMD simulations, and EOS models. Section III provides a comprehensive comparison of L21 with published results on He, as well as our own data. We conclude with some brief remarks in Sec. IV. Appendix A provides a concise summary of the EOS construction details.

## II. OVERVIEW AND METHODOLOGY

### A. Experimental materials and methods

To better constrain EOS models, we have conducted a series of shock-compression experiments to measure the Hugoniot state using Sandia National Laboratories’ Z-machine [31,32]. The Z-machine is a pulsed-power source capable of delivering  $\sim 26$  MA of current over a few 100 ns to a target. The large current produces a strong magnetic field, and the combined current and magnetic field generate a Lorentz force ( $\vec{F} = \vec{J} \times \vec{B}$ ) that accelerates an aluminum 6061-T6 flyer plate. The current pulse is carefully tailored to shocklessly accelerate the flyer plate to very high impact velocities and also maintain several hundred microns of solid density aluminum on the impact side of the flyer plate to produce a shock in the target [33–35]. The magnetically accelerated flyer technique has been successively refined and validated against conventional shock-compression techniques [36–38].

The helium target configuration is similar to targets successfully fielded on the Z-machine for shock-compression experiments on other cryogenic noble liquids xenon [39], krypton [40], and argon [41]. Figure 1 shows a schematic view of the experimental configuration. The target consists of a copper cell body with a z-cut  $\alpha$ -quartz drive plate, a copper spacer, and a z-cut,  $\alpha$ -quartz top-hat rear window. The copper spacer along with the quartz top-hat defined the ambient temperature sample thickness between the quartz drive plate and rear quartz top-hat. The gap between the quartz windows (approximately 300  $\mu\text{m}$ ) was filled with high-purity He gas (Matheson Trigas >99.9995%) to a pressure of 18.5 psi (1.27 bar). To reach liquid He temperatures, we used a conduction refrigerator with a vacuum pumped liquid He bath [42]. The target cell was connected to the liquid He reservoir

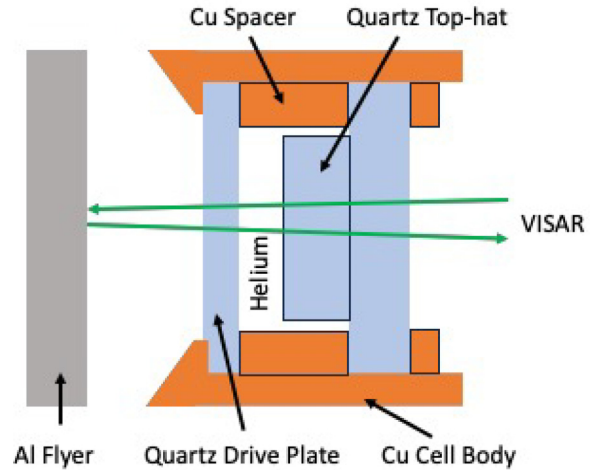


FIG. 1. Schematic illustration of the target geometry.

via a copper link. Once the reservoir filled with liquid He, a mechanical pump reduced the pressure above the He reservoir and began lowering the temperature of the liquid He in the reservoir. Using this method, we could reduce the temperature of the He gas in the target cell to below 4.2 K and completely fill the cell with liquid He. The target cell showed a change in pressure from 18.5 psi to approximately 17.6 psi (1.21 bar). Visual observation of target cells with identical fill volumes in offline testing showed that the target completely filled with liquid He and that the change in pressure was a reproducible marker to verify the transition to liquid He. The initial liquid He density was determined from density versus temperature data in Kerr [43] and ranged from 0.128 to 0.147  $\text{g}/\text{cm}^3$ .

A Velocity interferometry System for Any Reflector (VISAR) [44] measured the Al flyer velocities and shock velocities in the quartz drive plate, the helium sample, and the rear quartz window to within uncertainties of  $<0.8\%$ . We recorded multiple VISAR signals, each with a different velocity per fringe (VPF) to eliminate  $2\pi$  phase shift ambiguities in determining the shock velocities. We used the index of refraction for quartz ( $n = 1.547$ ) and the index of refraction for liquid He as a function of temperature from the data in Edwards [45] to correct the VPF in each material [38]. Additionally, integrating the shock velocity with respect to time verified that the distance was consistent with the sample thickness calculated using the Cu spacer thickness, its thermal contraction at liquid He temperature, and the quartz top-hat thickness. Figure 2 shows a typical analyzed VISAR trace from a Z experiment along with the raw data VISAR signal. With the transparent quartz windows, the 532 nm laser for the VISAR passes through the target cell and reflects off the Al flyer. The VISAR tracks the Al flyer velocity up to impact on the quartz drive plate. The shock causes the quartz to melt into a conducting fluid [38] and the VISAR directly measures the shock velocity ( $U_s$ ) as the shock transits the quartz. The shock front in the liquid He is also reflective, providing a direct, accurate measurement of the shock velocity. As the shock transits from the helium into the rear quartz tophat, the VISAR directly measures the shock velocity in the quartz tophat. The shock velocity measurement in the quartz

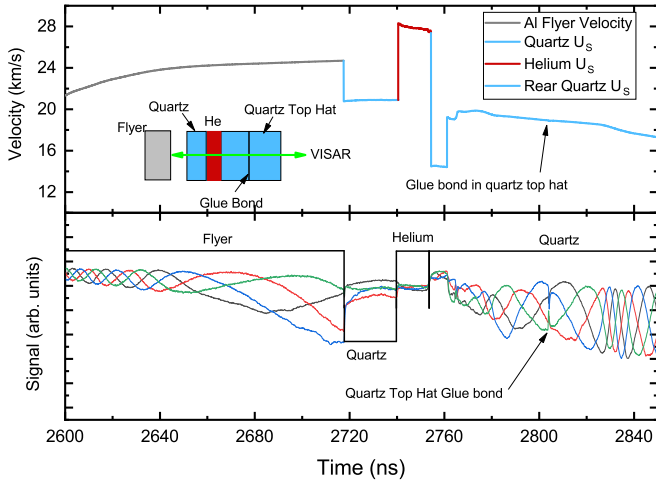


FIG. 2. VISAR trace from Shot Z3158 showing the flyer velocity and the shock velocities in the quartz drive plate, helium sample, and quartz rear window.

top hat shows jumps in velocity caused by reflected shocks originating from the interface between the quartz drive plate and the helium.

With the measured shock velocities, we determined the liquid He Hugoniot state using a Monte Carlo Impedance Matching method [47]. First, we determined the initial quartz Hugoniot state prior to the shock transiting into the He using the measured quartz shock velocity and the known Hugoniot for quartz [38,48,49]. In this case, we used the modified Universal Hugoniot fit presented in Knudson *et al.* [38,48,49]. The initial quartz density was  $2.65 \text{ g/cm}^3$  with an uncertainty of 0.3%. We then impedance matched to the Mie-Grüneisen, Linear Release (MGLR) quartz release model developed using deep release data on shocked quartz [48–50]. The Monte Carlo Impedance Matching method accounts for uncertainties in the measured shock velocities, initial densities, and the quartz model fit parameters. Table I lists the experimentally determined He Hugoniot data. Figure 3 plots our Hugoniot data alongside data from some representative studies. Section III provides a detailed analysis of these studies, as well as others not shown in the figure. Also plotted in the figure are our QMD simulation results (see Sec. II B) and Hugoniot curves from two EOS models mentioned in the Introduction: L20 [18–20] and S5764 [21]. Figure 3 shows that neither of these EOS models completely capture the QMD

TABLE I. Summary of our experimentally determined Hugoniot states for He initiated from cryogenic, liquid-phase initial conditions. In order from left to right, the columns indicate the shot label, the initial temperature  $T_0$ , the He initial density  $\rho_0$ , the He index of refraction, the shock speed  $U_s$  of the quartz window, and various information about the shock state achieved in He: its shock speed  $U_s$ , particle speed  $U_p$ , density  $\rho$ , and pressure  $P$ .

Shot	$T_0$ (K)	He $\rho_0$ ( $\text{g/cm}^3$ )	He Index	Quartz $U_s$ (km/s)	He $U_s$ (km/s)	$U_p$ (km/s)	$\rho$ ( $\text{g/cm}^3$ )	$P$ (GPa)
Z3158	4.06	$0.128 \pm 0.001$	1.026	$18.31 \pm 0.06$	$24.28 \pm 0.11$	$18.44 \pm 0.12$	$0.532 \pm 0.014$	$57.3 \pm 0.6$
Z2981	3.52	$0.135 \pm 0.001$	1.028	$24.68 \pm 0.06$	$34.48 \pm 0.28$	$26.96 \pm 0.16$	$0.619 \pm 0.024$	$125.5 \pm 1.2$
Z3050	2.64	$0.144 \pm 0.001$	1.029	$20.91 \pm 0.07$	$28.04 \pm 0.10$	$21.73 \pm 0.14$	$0.640 \pm 0.017$	$87.7 \pm 0.8$
Z2742	2.14	$0.147 \pm 0.001$	1.030	$22.02 \pm 0.11$	$29.60 \pm 0.16$	$23.18 \pm 0.19$	$0.678 \pm 0.025$	$100.9 \pm 1.1$

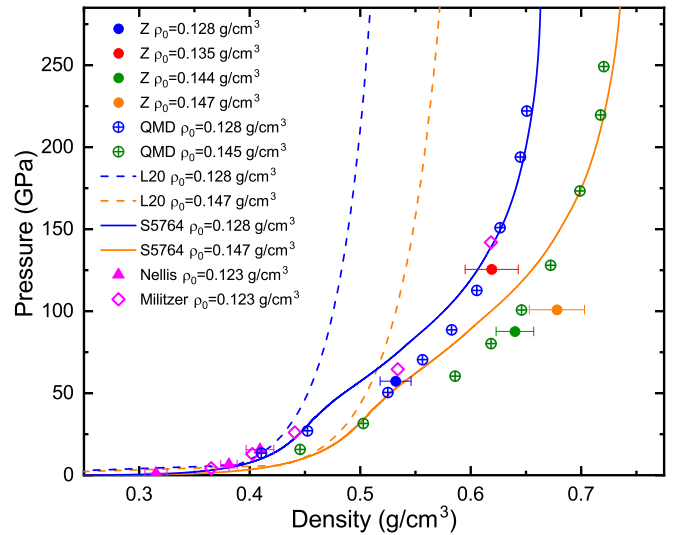


FIG. 3. Hugoniot data on fluid-phase helium. In this figure and all subsequent figures on the EOS, we list the name of only the first author due to space limitations. Here, we illustrate results from our Z-machine experiments and our QMD simulations, which we compare with experimental results from Nellis [27] and QMD simulations from Militzer [46]. The prior EOS models L20 (dashed curves) and S5764 (solid curves) are plotted for the bounding initial densities of 0.128 and  $0.147 \text{ g/cm}^3$ .

and experimental results. However, we reiterate that the earlier EOS models were made with limited lower-pressure experimental data and should not be expected to match the new data. The experimental and computational results prompted us to develop our L21 EOS for fluid-phase He that is discussed further in Secs. II C and III, and Appendix A.

## B. Density functional theory methods

Molecular dynamics based on *ab initio* density functional theory (DFT) [51,52] has demonstrated good agreement with equation of state data for materials at extreme conditions, and has a long history in this area in both shock-compressed solids and cryogenic liquids [38–41,50,53,54]. We have simulated shock-compression experiments by performing DFT-based QMD calculations using forces determined from the finite-temperature Mermin functional [55]. Tables II and III summarize our QMD results. We used PBE as the underlying exchange correlation functional [56]. All calculations were

TABLE II. Our QMD results (DFT-based MD simulations with the PBE functional) for the Hugoniot of fluid He with a  $T_0 = 4.06$  K,  $\rho_0 = 0.128$  g/cm<sup>3</sup> initial state.

$T$ (K)	$\rho$ (g/cm <sup>3</sup> )	$P$ (GPa)	$\rho/\rho_0$	$U_p$ (km/s)	$U_s$ (km/s)
10000	0.410(2)	13.49(4)	3.21(1)	8.52(2)	12.38(2)
20000	0.452(1)	27.00(5)	3.53(1)	12.30(1)	17.15(1)
35000	0.525(6)	51.0(5)	4.10(4)	17.4(1)	22.96(7)
42000	0.556(2)	70.4(2)	4.34(2)	20.58(3)	26.73(4)
50000	0.581(3)	88.5(4)	4.54(2)	23.22(5)	29.77(7)
60000	0.606(3)	112.0(3)	4.73(3)	26.27(4)	33.30(6)
75000	0.627(2)	153.5(4)	4.90(2)	30.89(4)	38.81(5)
90000	0.645(2)	195.8(3)	5.04(1)	35.02(3)	43.69(4)
100000	0.651(5)	222.2(6)	5.08(4)	37.38(4)	46.5(1)

performed with VASP 6.2.0 using the all-electron He *GW* pseudopotential [57,58], which has a PAW radius of 1.2 Å.

Extensive convergence studies were done, which were used to determine the following run parameters for our simulations [59]. Each simulation was run at the Baldereschi mean-value point with 128 atoms and a plane wave cutoff of 1400 eV. We ran isotherms at 10, 20, 35, 42, 50, 60, 75, 90, and 100 kK, with the time step varying between 0.2 fs and 0.01 fs at the highest temperatures. We used 10 uniformly spaced density points starting at 0.343 g/cm<sup>3</sup> and ending at 1.307 g/cm<sup>3</sup> for all isotherms except 10 kK, which included two additional density points starting at 0.272 g/cm<sup>3</sup>. The number of bands used for each isotherm was chosen to ensure adequate convergence, which corresponded to 1024 bands at 100 kK.

Equilibration was done at all considered densities along the 10 kK isotherm, which were then used to initialize the configurations at other temperatures. We removed the equilibration period for each simulation before accumulating thermodynamic averages. The length of the transient was between 0.1 and 0.5 ps, and the thermodynamic averaging was performed over roughly 1 ps, though was as short as 0.5 ps at the highest temperatures. All simulations used a velocity scaling NVT thermostat with a frequency of 100 time steps.

Nuclear quantum corrections to our reported isotherms were ignored, since the thermal DeBroglie wavelength is found to be significantly smaller than the average He–He

TABLE III. Our QMD results (DFT-based MD simulations with the PBE functional) for the Hugoniot of fluid He with a  $T_0 = 2.5$  K,  $\rho_0 = 0.145$  g/cm<sup>3</sup> initial state.

$T$ (K)	$\rho$ (g/cm <sup>3</sup> )	$P$ (GPa)	$\rho/\rho_0$	$U_p$ (km/s)	$U_s$ (km/s)
10000	0.455(3)	15.71(1)	3.13(2)	8.60(4)	12.63(5)
20000	0.503(2)	31.55(1)	3.47(1)	12.41(2)	17.44(2)
35000	0.586(2)	60.39(2)	4.04(2)	17.77(4)	23.61(3)
42000	0.618(3)	80.25(3)	4.26(2)	20.57(4)	26.87(4)
50000	0.645(2)	100.8(3)	4.45(2)	23.20(4)	29.93(4)
60000	0.672(1)	128.0(2)	4.64(1)	26.31(2)	33.55(2)
75000	0.699(5)	173.3(8)	4.82(3)	30.70(7)	38.7(1)
90000	0.717(5)	220(1)	4.95(4)	34.7(1)	43.5(1)
100000	0.723(11)	249(2)	4.99(8)	37.2(1)	46.5(2)

separation at all densities considered. However, due to the cryogenic conditions of our reference points, we estimated nuclear quantum corrections to both the initial state energies and pressures to determine if they had any effect on our computed Hugoniot. We did this by using path-integral molecular dynamics to compute the nuclear quantum corrections to both the energy and the pressure. Due to the very good accuracy of classical pair potentials for modeling helium at low pressures and temperatures, we used classical exponential-six potentials in lieu of a full-DFT solve for the assessment of nuclear quantum effects. Specifically, the He–He interaction is given by

$$\phi_{Exp-6}(r) = \frac{\epsilon}{\alpha - 6} \left\{ \exp \left[ \alpha \left( 1 - \frac{r}{r^*} \right) \right] - \alpha \left( \frac{r^*}{r} \right)^6 \right\}, \quad (1)$$

where  $\epsilon/k_b = 10.57$  K,  $r^* = 2.97$  Å, and  $\alpha = 13.6$ . These specific parameters were taken from existing work in the area [60]. All PIMD calculations were performed using i-PI [61] with LAMMPS [62] as the force calculator.

Sixty-four time slices were found to be sufficient to converge the kinetic energy, potential energy, and pressure to less than 1% in the PIMD simulations. We have conducted simulations to calculate Hugoniot curves from two different initial states (reference points): (1)  $T_0 = 2.5$  K,  $\rho_0 = 0.145$  g/cm<sup>3</sup> and (2)  $T_0 = 4.06$  K,  $\rho_0 = 0.125$  g/cm<sup>3</sup>. The nuclear quantum corrections to the energy and pressure were found to be 4.3 meV/atom and 27.6 bar for the 2.5 K reference point, and 3.91 meV/atom and 19.8 bar for the 4.06 K reference point. These corrections are negligible, but we added these corrections onto the PBE-based QMD simulations with classical nuclei for the 2.5 K and 4.06 K reference points, respectively, and the resulting Hugoniot curves are summarized in Tables II and III. Due to the extreme temperatures and relatively modest densities for this work, nuclear quantum effects are not included anywhere else except at the reference points.

### C. EOS models

Like in previous EOS work on other materials [21,28–30,63–68], we represent the EOS of He in terms of its Helmholtz energy  $F$  as a function of temperature  $T$  and density  $\rho$ , and we divide  $F$  into three contributions:

$$F(T, \rho) = F_{\text{cold}}(\rho) + F_{\text{ion}}(T, \rho) + F_{\text{electron}}(T, \rho), \quad (2)$$

where  $F_{\text{cold}}(\rho)$ ,  $F_{\text{ion}}(T, \rho)$ , and  $F_{\text{electron}}(T, \rho)$  are the cold, ion-thermal, and electron-thermal contributions, respectively. The physical meaning of each term, and particular models we have used are explained in the earlier studies [21,28–30,63–68], and so we give only a brief description here.

The cold energy  $F_{\text{cold}}(\rho)$  designates the energy of He at 0 K and is often referred to as the cold curve since it depends on only one independent variable (i.e.,  $\rho$ ). It excludes thermal motion of the nuclei, and instead reflects the potential energy in the ground-state electronic configuration, as well as the zero-point energy. We represent the cold curve as a series of cubic splines [69] on which we employ a piecewise-smoothing procedure (localized fits to analytical EOS models or polynomials) to reduce some of the numerical noise. In the

case of a fluid, the cold curve is a theoretical construct since it is not the stable phase at 0 K, notwithstanding the ultra low-temperature superfluid He that is not even considered in our EOS. Nevertheless, it is useful to include  $F_{\text{cold}}(\rho)$  in our formulation because out of the three free-energy terms in Eq. (2), it makes the largest contribution to the total free energy at the intermediate densities and low temperatures where static compression experimental data collected on fluids are available. For fluid He, we have room-temperature isotherm experiments [22–25,70] that span a range from about 0.1–1.0 g/cm<sup>3</sup>. We adjust the splines in this density range to give a good representation of that set of experimental data. Below this intermediate range, the cold curve is stitched to a soft-sphere model [28,63,64] whose coefficients are adjusted to give a reasonable critical temperature, though an accurate representation of critical properties and the vapor-liquid dome is not the focus of the present study.

At higher densities, the cold curve is extrapolated to agree with predictions from the PURGATORIO code [71,72]. PURGATORIO employs an atom-in-jellium model, which it solves through all-electron, relativistic DFT calculations. Like the Thomas-Fermi model [63], PURGATORIO asymptotically approaches the limit of a one-component plasma [73] at high densities, but it includes additional physics (e.g., accounting for shell structure) that are neglected in Thomas-Fermi, and so it yields generally more accurate behavior below the one-component-plasma limit. For this reason, we utilize PURGATORIO to also calculate the electron-thermal contribution  $F_{\text{electron}}(T, \rho)$ , which represents thermally activated processes like electronic excitation, ionization, and recombination events. We obtain the electron-thermal free energy  $F_{\text{electron}}(T, \rho)$  by subtracting PURGATORIO’s prediction for the cold energy from its prediction of the total free energy:  $F_{\text{electron}}(T, \rho) = F_{\text{purgatorio}}(T, \rho) - F_{\text{purgatorio}}(T = 0, \rho)$ . An undesired byproduct of performing this subtraction is that it creates numerical pathologies at lower temperatures and densities, which we resolve with the empirical “cleanup” procedure described in our earlier study on a beryllium EOS [29].

The ion-thermal term  $F_{\text{ion}}(T, \rho)$ , which accounts for the motion of the ions (the positively charged nuclei), presents the most interesting challenges in terms of the construction of L21. It plays an important role at moderately high temperature and density states, such as those along the shock Hugoniot where He still behaves like an ordinary liquid (and not an ionized plasma dominated by the electron-thermal term). Initially, we tried to represent  $F_{\text{ion}}(T, \rho)$  with the Cell model developed by Correa *et al.* [29,30,74], which we have previously applied to fluid phases in metallic systems [29,30]. However, we found the Cell model always resulted in Hugoniot too compressible (i.e., it yields too large of a density for a given pressure along the Hugoniot) compared to the experimental and theoretical studies. In retrospect, this is understandable given that the Cell model is partly inspired from previous atomistic studies on the liquid phase of dense metals [65–67], and He atoms interact through weak van der Waals forces rather than the delocalized electron sea that characterizes typical metallic bonds. Thus, to model  $F_{\text{ion}}(T, \rho)$  in He, we have instead turned to the Cowan model [28,63], which is

a legacy model developed over 40 years ago [75] to describe fluids.

The Cowan model treats a fluid as if it were a dense, nonideal gas where the perturbative correction term scales as a function of the ratio of the temperature to the corresponding melt temperature at the given density [63]. The temperature ratio is a measure of the intensity of the interatomic interactions, with higher temperatures signifying weaker interactions. This physical picture encapsulated in the Cowan model seems to be more representative of the nature of van der Waals interactions, and this is reflected in our ability to construct a reasonably accurate fluid-phase He EOS with it. We use the Cowan prescription described by More *et al.* [63], in which

$$F_{\text{ion}}(T, \rho) = F_{\text{Cowan}}(T, \rho) = \frac{k_{\text{B}}T}{M} f(u, w), \quad (3)$$

where  $k_{\text{B}}$  is the Boltzmann constant,  $M$  is the molar mass, and the dimensionless function  $f = f(u, w)$  is defined in terms of two dimensionless variables,  $u = \theta/T$  and  $w = \alpha\theta^2/(\rho^{2/3}T)$ , as

$$f = -\frac{11}{2} + \frac{9}{2}w^{1/3} + \frac{3}{2}\ln\left(\frac{u^2}{w}\right). \quad (4)$$

Here,  $\alpha$  is a material-specific constant and  $\theta = \theta(\rho)$  is a density-dependent Debye temperature. The Debye temperature  $\theta(\rho)$  serves as an adjustable function that we calibrate to available Hugoniot data and other properties of interest. It is closely associated with the ion-thermal Grüneisen parameter  $\gamma_{\text{ion}}$  through the relation  $\gamma_{\text{ion}}(\rho) = d \ln \theta / d \ln \rho$ . It can be shown [63] that  $F_{\text{Cowan}}$  approaches the appropriate ideal-gas limit at high temperatures where  $T \gg T_{\text{m}}$ .

### III. RESULTS AND DISCUSSION

As discussed in Sec. II C, the L21 EOS involves two adjustable terms, the cold energy  $F_{\text{cold}}(\rho)$  and the ion-thermal Grüneisen parameter  $\gamma_{\text{ion}} = \gamma_{\text{ion}}(\rho)$ , both of which we treat as functions of density  $\rho$  only. Sections III A–III C describe how the available experimental data, including our own shock-compression experiments presented in Sec. II A, constrain  $F_{\text{cold}}(\rho)$  and  $\gamma_{\text{ion}}(\rho)$ . In particular, Sec. III A focuses on the room-temperature isotherm experiments that serve mainly to constrain  $F_{\text{cold}}(\rho)$ , while Secs. III B and III C describe how dynamic-compression experiments constrain  $\gamma_{\text{ion}}(\rho)$ . The last section, Sec. III D, compares the EOS to other published results that we have not used to constrain the EOS and instead serve as “holdouts” to test the EOS performance. Appendix A presents a focused summary of the EOS and a concise description of how we have fit  $F_{\text{cold}}(\rho)$  and  $\gamma_{\text{ion}}(\rho)$ .

#### A. Room-temperature isotherm

Figure 4 shows results for the pressure versus density along the room-temperature ( $\approx 297$  K) isotherm. The experimental data, which are inferred from sound-speed and refractive-index measurements, suggest that L20 [18–20] is too soft, while the astrophysical EOSs—a grouping that includes SCvH [8], Chabrier *et al.* [10], and Becker *et al.* [9]—are too stiff. These EOSs feature an amalgamation of different models that are stitched together to collectively account for phe-

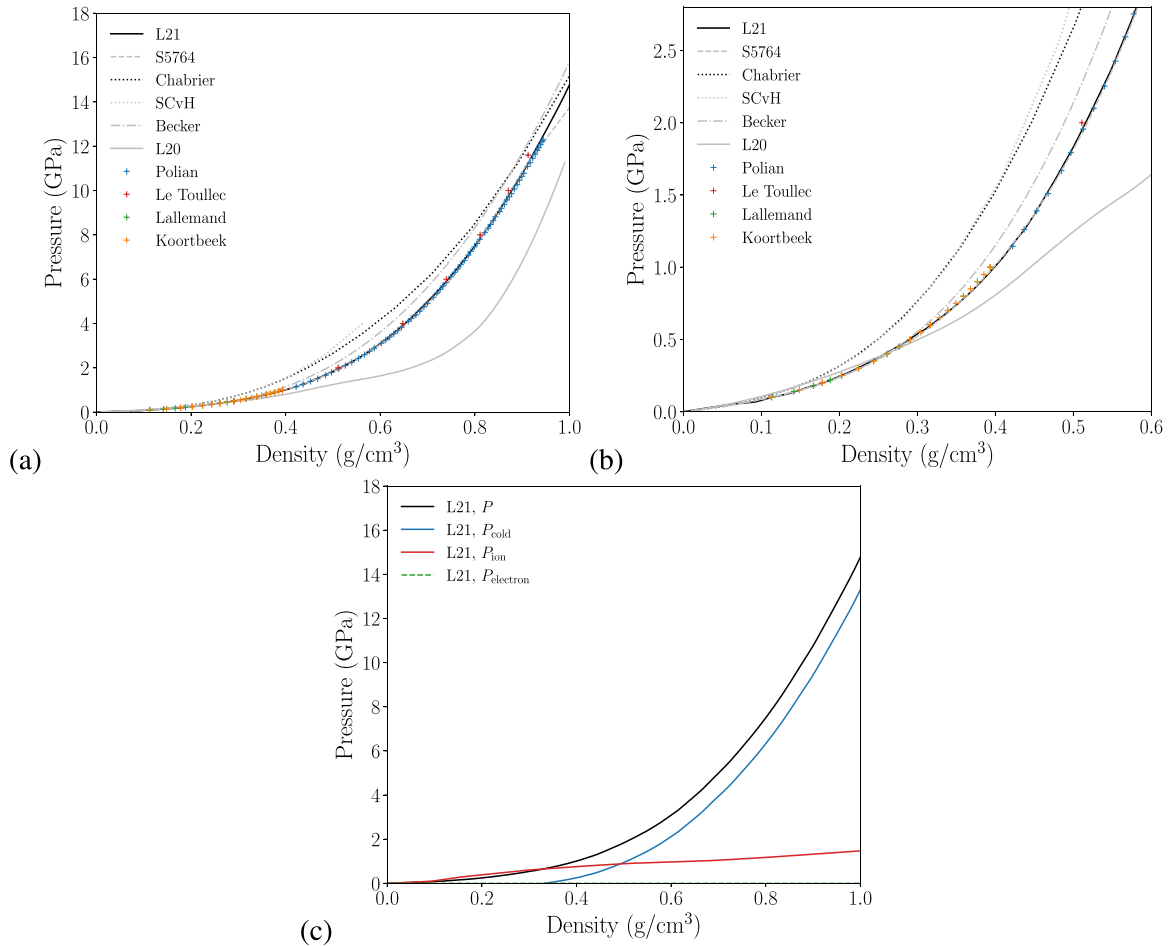


FIG. 4. The room-temperature isotherm of He from our L21 EOS, various other EOS models (S5764 [21], Chabrier *et al.* [10], SCvH [8], Becker *et al.* [9], L20 [18–20]) and experimental data [22–25]: (a) complete range over which the fluid is thermodynamically stable; (b) magnified view of (a); (c) comparison of the different pressure contributions to the total pressure  $P = P_{\text{cold}} + P_{\text{ion}} + P_{\text{electron}}$  in L21 along the isotherm, in which we compute all of these terms in a self-consistent manner by evaluating volumetric derivatives of the Helmholtz energy  $F$  in Equation (2) [i.e.,  $P = -(\partial F/\partial V)_T = -(\partial F_{\text{cold}}/\partial V)_T - (\partial F_{\text{ion}}/\partial V)_T - (\partial F_{\text{electron}}/\partial V)_T$ ]. As stated in the text, the electron-thermal contribution to  $F$  and  $P$  is virtually zero at room temperature.

nomena like nuclear quantum effects, interatomic interactions (including electrostatic screening), and electronic excitations, but at the particular conditions along the room-temperature isotherm, all of these EOS models essentially reduce to an ideal-gas term plus some type of configurational term (e.g., a virial series expansion, or an integral over a product of a pair-correlation function with an interatomic potential) that corrects for nonideal interactions. Soft behavior indicates that the EOS overestimates the strength of attractive interactions between atoms, leading to an overly compressible, dense fluid. On the opposite end, a stiff EOS underestimates the strength of the attractive interactions, leading to an underdense fluid. In contrast, both S5764 [21] and our L21 EOS are designed to agree with the experimental data, suggesting a proper balance of attractive-to-repulsive interactions. Thus, out of the EOSs depicted in Fig. 4, these two models are the ones most suitable for applications involving He at room temperature or relatively close to room temperature (say, within a few hundred degrees), such as the studies mentioned in the Introduction that have examined compressed He bubbles to probe the effects of aging in nuclear reactors [3–7]. We will henceforth

focus primarily on S5764 and the Chabrier *et al.* EOS (this last one being the latest SCvH-like EOS currently available) when comparing L21 with other EOS models.

For a typical solid, the room-temperature isotherm is determined almost completely by the cold energy  $F_{\text{cold}}(\rho)$  and is virtually unaffected by the other two free-energy terms in Eq. (2). However, for a fluid, especially the fluid phase of a light element like He, the ion-thermal term  $F_{\text{ion}}(T, \rho)$  makes a non-negligible contribution to the behavior of the EOS along the isotherm at lower densities (although the electron-thermal term  $F_{\text{electron}}$  is virtually zero at room temperature), as shown in Fig. 4(c). This complicates the EOS-construction process because it introduces a coupling between  $F_{\text{cold}}$  and  $F_{\text{ion}}$ . Nevertheless, the temperature of the isotherm is low enough that it is still largely a reflection of  $F_{\text{cold}}$ . We have adopted an iterative procedure whereby we adjust  $F_{\text{cold}}$  to match the data along the isotherm, then tune  $F_{\text{ion}}$  to agree with data for other properties of interest presented later in this paper (e.g., Hugoniot curves), then revisit the isotherm and make small refinements to  $F_{\text{cold}}$  to account for the newly modified  $F_{\text{ion}}$ , and so forth, until we are able to reproduce the data for all desired properties.

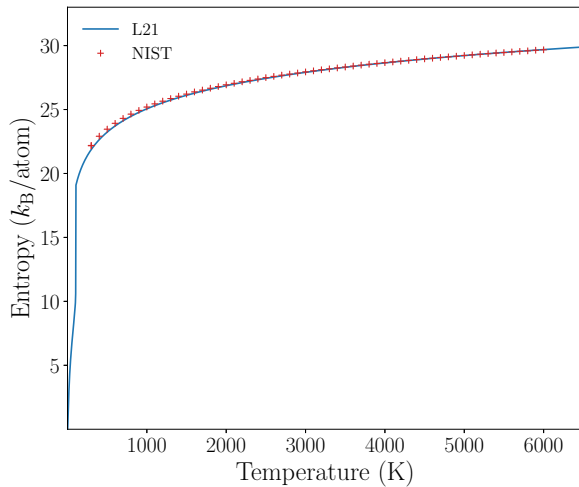


FIG. 5. Comparison of the ambient-pressure entropy (He is a gas along the conditions shown in this figure) of L21 with data obtained from the National Institute of Standards and Technology (NIST) database, which comes from a multiparameter EOS designed for low-pressure industrial applications [12].

### B. Shock compression up to 1 g/cm<sup>3</sup> and ambient-pressure entropy

We now turn our attention to the ion-thermal term  $F_{\text{ion}}$ , which is specified by setting the density dependence of the ion-thermal Grüneisen parameter  $\gamma_{\text{ion}}(\rho) = d \ln \theta(\rho) / d \ln \rho$  and a value  $\theta_{\text{ref}}$  for the Debye temperature  $\theta(\rho)$  at a particular reference density  $\rho_{\text{ref}}$ . We fit the latter to data on the ambient-pressure entropy in the gas phase (Fig. 5). The Grüneisen parameter  $\gamma_{\text{ion}}$  is fit to various dynamic-compression data, notably Hugoniot curves obtained through shock-compression experiments. These experiments provide convenient constraints because they allow us to largely separate the cold energy from the thermal terms in Eq. (2) when constructing the EOS. This is because they access high-temperature conditions where the cold energy makes only a small contribution so that the total free energy is instead largely a reflection of the ion-thermal term, and possibly also the electron-thermal term at sufficiently high temperatures (for strong enough shocks). Since  $\gamma_{\text{ion}}(\rho)$  is a function of only  $\rho$  in our models, we divide the dynamic-compression data according to the density range that they access. The dynamic-compression data that we discuss in the present subsection (Sec. III B) provide constraints on  $\gamma_{\text{ion}}(\rho)$  at densities below 1 g/cm<sup>3</sup>, while the data discussed in Sec. III C provide constraints on  $\gamma_{\text{ion}}(\rho)$  at densities above 1 g/cm<sup>3</sup>.

We start with Fig. 6, which features two sets of shock-compression experiments: (1) our experiments described in Sec. II A and (2) those presented by Seagle *et al.* [76]. These two sets of experiments access the same range of densities, up to about 0.7 g/cm<sup>3</sup>, although they probe quite different temperatures and pressures, owing to the different initial states that they examine. Also included in Fig. 6 are results from our QMD simulations described in Sec. II B. S5764 yields Hugoniot curves in the illustrated density range that appear to be too stiff, implying that it overestimates  $\gamma_{\text{ion}}$  so that its ion-thermal pressure is too high for a given density. As a

result, the Hugoniot temperatures from S5764 must also be notably higher than those from L21 throughout most of the density range (assuming that the heat capacities  $C_V$  from the two EOSs are comparable in this range, which is the case) in order to satisfy the Rankine-Hugoniot equation

$$E - E_0 = \frac{1}{2}(P + P_0)(V_0 - V), \quad (5)$$

where  $E_0$ ,  $P_0$ , and  $V_0$  are the initial internal energies, pressures, and volumes corresponding to the initial temperatures  $T_0$  and densities  $\rho_0$  listed in the figure. The discrepancy is more prominent in our experiments [Figs. 6(a), 6(c), and 6(e)], where the predictions from S5764 lie outside of the error bars for three out of our four shots. We have also performed Hugoniot calculations with the Chabrier *et al.* EOS [10], but we do not show its results in the figure because that EOS does not agree at all with the Seagle *et al.* experiments (it is far stiffer than S5764), which involve room-temperature initial states. We have not attempted to perform calculations for our experiments with the Chabrier *et al.* EOS because the lowest temperature in their EOS table is 100 K, which is above that of the cryogenic initial states in our experiments.

We have constructed our L21 EOS to fall within the error bars of both sets of experiments. The agreement is imperfect, however, as the data suggest that our EOS is perhaps a little on the stiff side for our shock-compression experiments (especially at higher pressures), while it may be somewhat on the soft end for the Seagle *et al.* experiments. The results in Fig. 6 represent a reasonable compromise with satisfying the opposing demands from these two sets of experiments. In order to further improve the agreement, one would need to either adopt a different electron-thermal model from our choice of PURGATORIO, and/or assume that  $\gamma_{\text{ion}}$  is a function of both temperature and density. (We note that although the ion-thermal Grüneisen parameter  $\gamma_{\text{ion}}$  in L21 depends on density only, the total Grüneisen parameter in the EOS is, in fact, a function of  $T$  as well because the electron-thermal term introduces a temperature dependence.) All of these modifications would introduce additional challenges such as ensuring that adopting a particular temperature-dependent  $\gamma_{\text{ion}}$  still allows the ideal-gas limit to be satisfied.

Figure 7 portrays results for the shock-compression experiments performed by Nellis *et al.* [27]. Like in our experiments, they start from a cryogenic initial temperature  $T_0$  of about 4 K. Their initial density  $\rho_0$  of about 0.123 g/cm<sup>3</sup> is comparable to the lowest initial density in our experiments, but their final shock states are lower in pressure. In addition, Nellis *et al.* performed a double-shock experiment in which a shock state at a density of about 0.41 g/cm<sup>3</sup> on the  $T_0 \approx 4$  K Hugoniot is subjected to a second shock wave. By design, both L21 and S5764 agree well with the single-shock experimental data shown in blue in Fig. 7. Additionally, S5764 falls within the error bars of the double-shock experiment, while L21 is too soft. It is not possible to adjust  $\gamma_{\text{ion}}$  in L21 to agree with the double-shock experiment without significantly worsening the agreement for the Hugoniot data in Figure 6. For example, the data point for the double-shock experiment is centered at a density that is similar to those of the orange and green experimental points in Figs. 6(a) and 6(b), respectively. Comparing these three data points, one can see that it is difficult to develop a model that agrees with all three of them. S5764

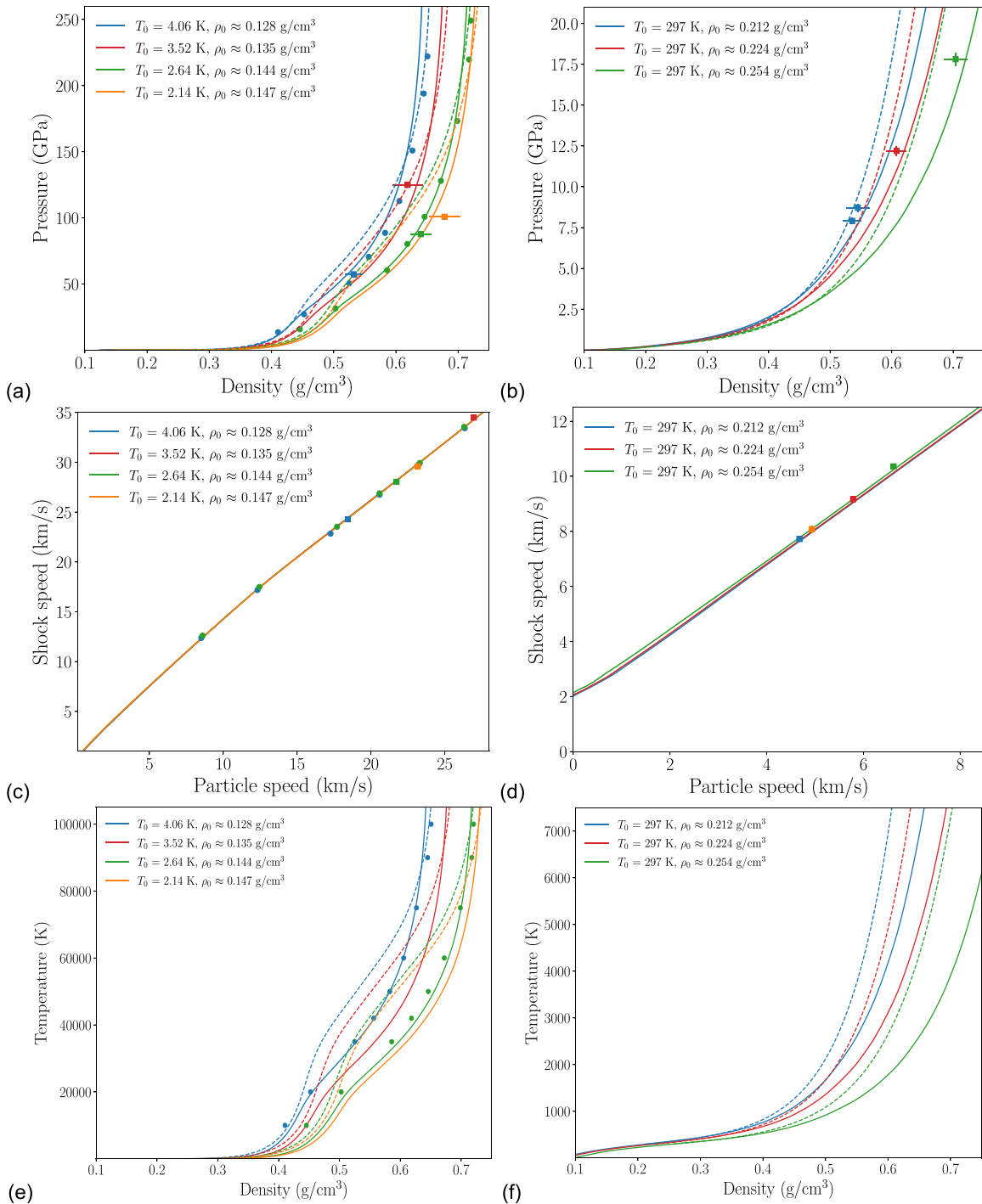


FIG. 6. Comparison of the Hugoniot curves examined by our shock-compression experiments [(a), (c), and (e)], in which the initial states are cryogenic liquids, with the Hugoniot curves examined by Seagle *et al.* [76] [(b), (d), and (f)], in which the initial states are precompressed fluids at room temperature: [(a) and (b)] pressure vs density; [(c) and (d)] shock speed vs particle speed; and [(e) and (f)] temperature vs density. The different initial conditions and their associated curves/symbols are colored according to the scheme shown in the legends. The solid curves, dashed curves, squares, and circles represent our L21 EOS, the S5764 EOS [21], experimental data (with the lines extending out from the squares indicating error bars), and our QMD simulations, respectively.

noticeably overpredicts the pressure for both the orange and green data points, yet despite that, it may still be somewhat underpredicting the pressure for the Nellis *et al.* double-shock data point since it falls near the edge of the experimental uncertainties for that particular point on the soft side. We note that a recent study on argon [41] also demonstrated that

EOS models have difficulties in matching reshock states off of the principal Hugoniot. Employing more sophisticated models could possibly improve the performance in the off-Hugoniot states. However, it may also be possible that inconsistencies exist among the data and that further experimental work to measure the reshock states in He are needed.

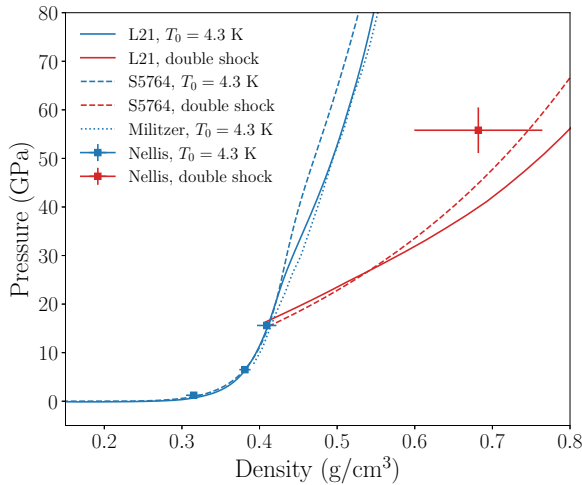


FIG. 7. Pressure vs density for the shock-compression experiments conducted by Nellis *et al.* [27]. Results for the single-shock experiments are colored in blue, while those for the double-shock experiment are in red. The theoretical results in this figure are taken from the L21 and S5764 [21] EOS models, as well as *ab initio* simulations performed via path-integral Monte Carlo and QMD by Militzer [46].

Unlike the previous shock-compression experiments considered so far, which feature liquid-phase (or liquidlike supercritical fluid) initial states, the initial states examined by Cai *et al.* (Fig. 8) are all gaslike states. They have performed experiments where He is shocked from a temperature of 293 K and one of three different pressures: 6, 12, and 50 bar. These different initial states lie close enough to each other that the resulting shock states can all be described by the same linear shock speed-particle speed ( $U_s-U_p$ ) relation within the experimental uncertainties. The densities spanned by their experiments cover a range of about 0.001–0.01 g/cm<sup>3</sup>, and they are therefore useful in constraining  $\gamma_{\text{ion}}$  in this low-density regime. We have been able to adjust  $\gamma_{\text{ion}}$  in L21 to give good

agreement to the experimental  $U_s-U_p$  data, but our resulting shock temperatures lie on the low end of the range spanned by the data. However, Cai *et al.* do not report uncertainties in their temperature data. Given the difficulties in measuring temperature in shock-compression experiments, it is not unreasonable to assume error bars of at least  $\pm 10\%$ , as shown in Figs. 9 and 11 below. If we assume this level of uncertainty, L21 would fall within the error bars of most of the points.

### C. Shock compression and quasi-isentropic compression beyond 1 g/cm<sup>3</sup>

Figure 9 presents Hugoniot results for laser-driven shock-compression experiments [78–80]. The final shock pressures and densities attained in these experiments were originally reported by Eggert *et al.* [79], while Celliers *et al.* [80] reported the corresponding shock temperatures obtained through pyrometry. The setup in these experiments involve a quartz plate that serves as a reference to enable a determination of the shock velocities. Brygoo *et al.* [78] later reanalyzed the results reported by Eggert *et al.* and Celliers *et al.* with a new quartz release model, and it is this corrected set of data that we examine in Fig. 9. These experiments are similar to Seagle *et al.* [76] in that they involve initial states where fluid He is precompressed at room temperature, but they cover a broader range of initial densities and also access much higher shock pressures of up to about 200 GPa. For the purposes of comparison, we have included a few data points from Seagle *et al.*, which are depicted by the green circles in Fig. 9. Discussions in earlier studies [78–82] have pointed out that at lower initial densities, the first-principles simulations by Militzer [46,81] and Preising *et al.* [82] are stiff compared to Brygoo *et al.*, but that the agreement with experiment tends to get progressively better with increasing precompression. It is perhaps not surprising then that L21 and S5764 display similar behavior with respect to Brygoo *et al.*, since we have seen from Fig. 7 that L21, S5764, and Militzer all lie rather close to each other for the Nellis *et al.* Hugoniot. Interestingly, the

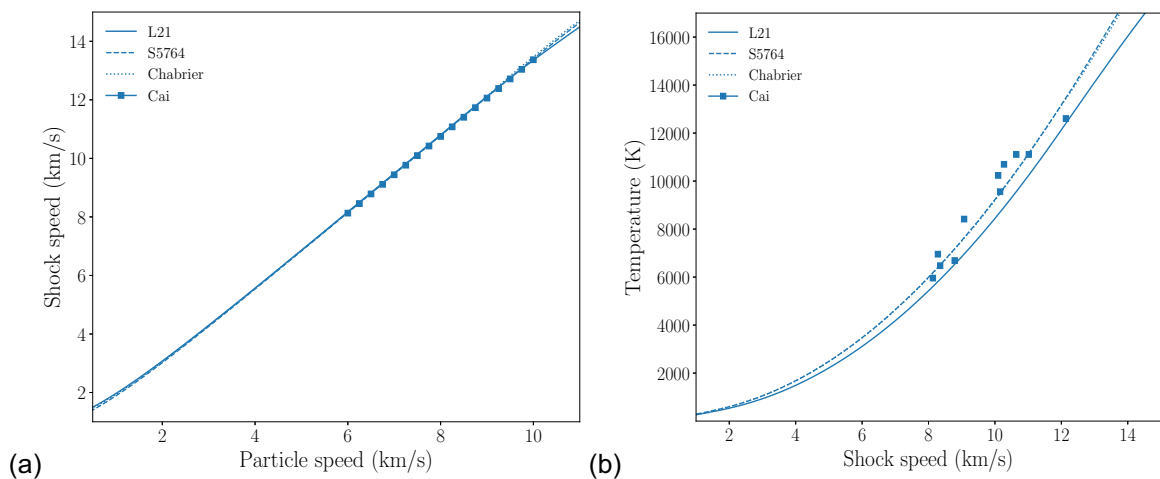


FIG. 8. Results for shock-compression experiments performed by Cai *et al.* [77]: (a) shock speed vs particle speed and (b) temperature vs shock speed. The solid curves, dashed curves, dotted curves, and squares represent L21, S5764 [21], the Chabrier *et al.* EOS [10] (which overlaps closely with S5764 for this particular data set), and the experimental data, respectively. The Hugoniot curves from the EOS models are computed from an initial temperature and pressure of 293 K and 20 bar, respectively.

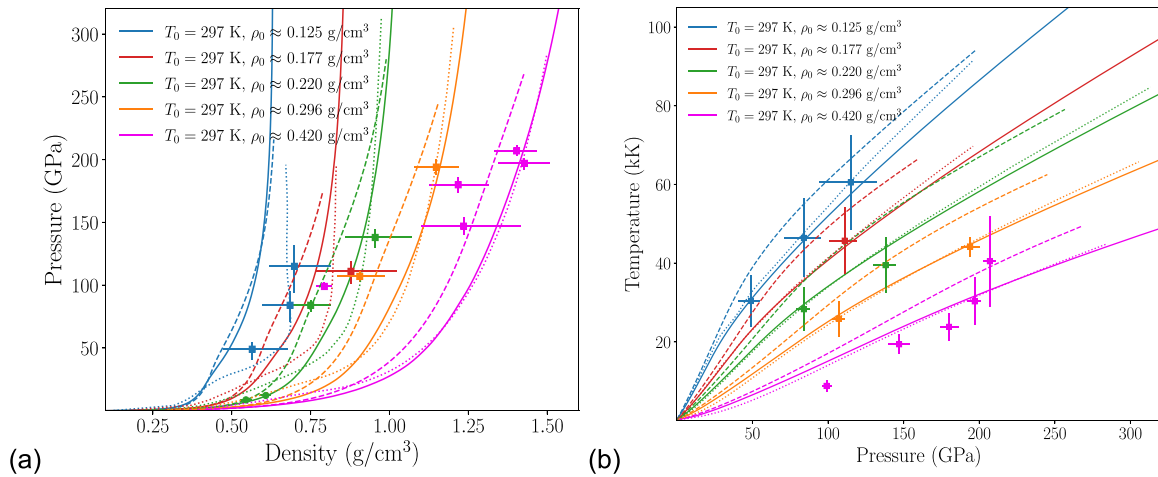


FIG. 9. Results for shock-compression experiments reported by Brygoo *et al.* [78], who have reanalyzed the original set of results for these experiments that were originally published by Eggert *et al.* [79] and Celliers *et al.* [80]: (a) pressure vs density and (b) temperature vs pressure. The different initial conditions and their associated curves/symbols are colored according to the scheme shown in the legends. The solid curves, dashed curves, dotted curves, and squares represent L21, S5764 [21], the Chabrier *et al.* EOS [10], and experimental data from Brygoo *et al.*, respectively. The green circles below 20 GPa in (a) are three experimental data points from Seagle *et al.* [76] where the initial densities [0.212–0.224 g/cm<sup>3</sup>; see Fig. 6(b)] are close to 0.220 g/cm<sup>3</sup>.

Chabrier *et al.* EOS significantly overpredicts the pressure for Seagle *et al.* [as can be seen in Fig. 9(a) and as stated in our discussion of Fig. 6(b)], but it seems to provide slightly better overall agreement with Brygoo *et al.* in pressure-density space than does L21 or S5764, although none of these EOS models are able to pass through the error bars of all the data points. The uncertainties on the shock temperatures are large enough that they cannot clearly discern a “best” EOS, though the temperatures from S5764, which are portrayed by the dashed curves, lie outside of (above) the error bars of all the green

and orange data points in Fig. 9(b). Further experiments with improved precision would help further constrain the models in this region.

At much higher densities, we consider the data illustrated in Fig. 10, which features results reported by Mochalov *et al.* [83–88] and Zhernokletov *et al.* [89,90]. Over several publications spanning nearly a decade, Mochalov *et al.* have performed experiments in which fluid He in a spherical chamber is compressed by a series of multiple, reverberating shocks. This type of multiple-shock compression typically results in a quasi-isentropic loading path that crosses through the initial temperature and density. But in their experiments, the entropy generated during the first shock is so large that the He more closely follows a shock-ramp path in which the second, third, fourth, etc. shock states define a quasi-isentrope that is initiated from the first shock state. Figure 10 shows this quasi-isentropic portion of their loading path. Also included in this figure are data from Zhernokletov *et al.*, who have performed similar experiments and analyses. The data reported by these studies are not derived purely from experiments, but rather are obtained by applying theoretical models to experimental data. More specifically, the density is estimated by examining through x-ray imaging how the geometry of the spherical chamber (i.e., its radius) changes with compression, while the pressure is computed through hydrodynamic simulations and EOS models. Mochalov *et al.* [88] report that an isentrope computed from their EOS that is initiated from an assumed first-shock state of  $\rho_0 = 1.45$  g/cm<sup>3</sup> and  $P_0 = 188$  GPa is able to give a good representation of their data. The other EOSs in Fig. 10 yield roughly the same results for that isentrope. Although the data points in the figure were not obtained purely through experimental means, we still consider them in the construction of our EOS because they are the only results currently available for He at relatively high densities that involve some form of experimental measurements, and thus to some degree, they provide constraints on the high-density behavior of the EOS.

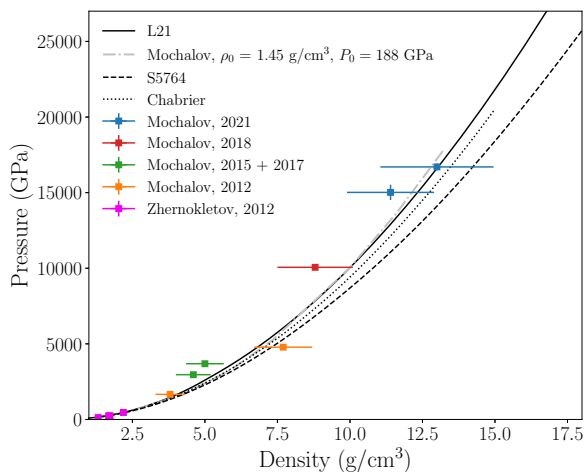


FIG. 10. Pressure vs density along the quasi-isentropic loading path in the multiple-shock-compression studies of Mochalov *et al.* [83–88] and Zhernokletov *et al.* [89,90]. The gray dashed–dotted curve depicts the isentrope that Mochalov *et al.* [88] have computed with their EOS. This isentrope passes through the  $\rho_0$  and  $P_0$  indicated in the legend, which is the density and pressure of the shock state from which the isentrope is initiated. The other curves are calculations of that same isentrope with L21, S5764 [21], and the Chabrier *et al.* EOS [10].

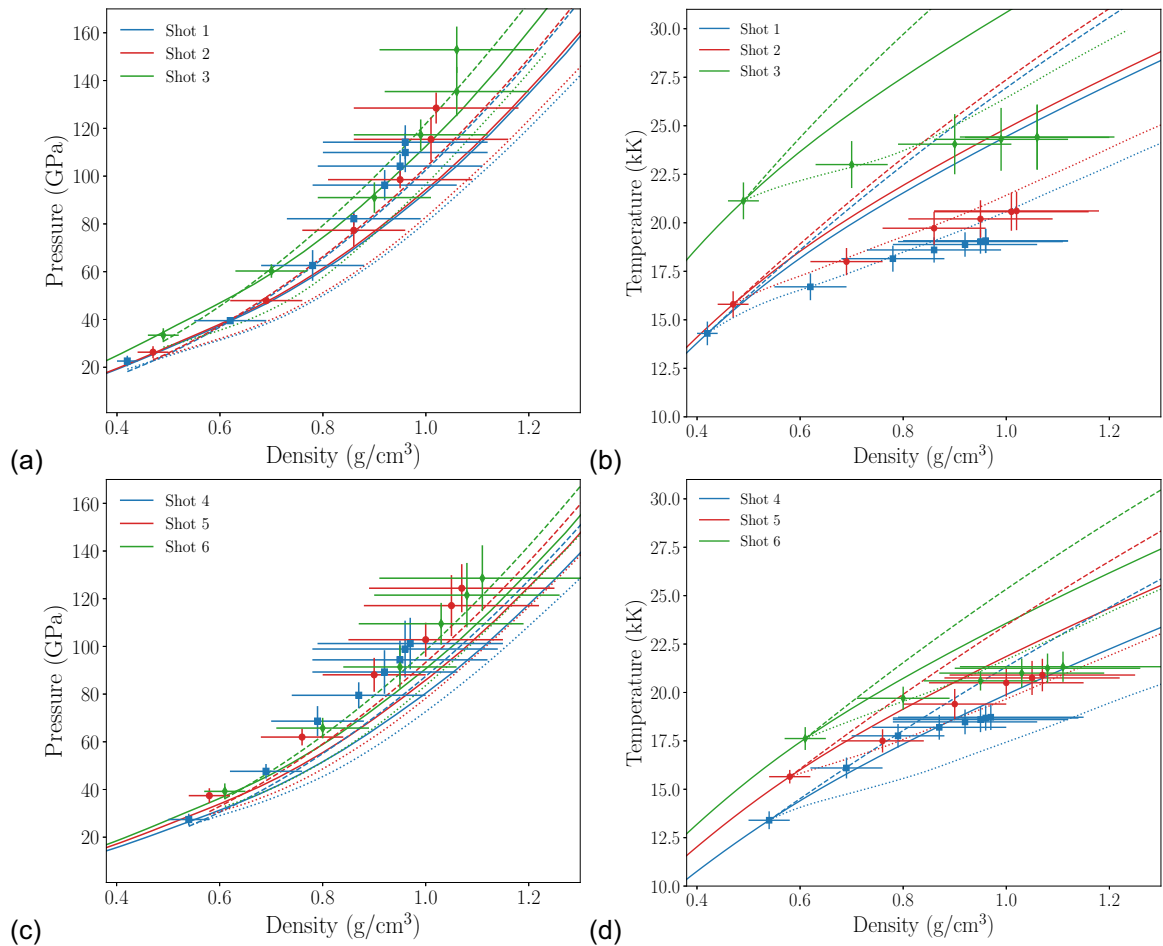


FIG. 11. Results for the quasi-isentropic loading path in the multiple-shock-compression studies of Zheng *et al.* [91]: [(a) and (b)] pressure vs density and temperature vs density in shots 1, 2, and 3, where the initial states are at room temperature and a density of  $0.03 \text{ g/cm}^3$ ; [(c) and (d)] pressure vs density and temperature vs density in shots 4, 5, and 6, where the initial states are at room temperature and a density of  $0.05 \text{ g/cm}^3$ . The different shots and their associated curves/symbols are colored according to the scheme shown in the legends. The solid curves, dashed curves, dotted curves, and symbols represent L21, S5764 [21], the Chabrier *et al.* EOS [10], and experimental data from Zheng *et al.*, respectively. The curves generated from the EOS models are isentropes that pass through the temperature and density of the leftmost points in (b) and (d).

#### D. Comparison to other experimental data and theoretical results

With the two adjustable functions  $F_{\text{cold}}(\rho)$  and  $\gamma_{\text{ion}}(\rho)$  in our EOS having now been determined, we compare the resulting EOS to other published data that were not used to constrain our EOS and instead serve as a holdout to further test the EOS. Figure 11 shows results from Zheng *et al.* [91], who have performed a set of six experiments where fluid He initially precompressed to either  $0.03 \text{ g/cm}^3$  (shots 1, 2, 3) or  $0.05 \text{ g/cm}^3$  (shots 4, 5, 6) at room temperature is subjected to a series of 8–10 reverberating shock waves. Similar to the behavior exhibited in the multiple-shock experiments of Mochalov *et al.* described above, Zheng *et al.* find that the first three shocks in each of their shots generates a non-negligible amount of entropy, while the path mapped out by the subsequent shocks can be roughly thought of as an isentrope that passes through the third shock state. Figure 11 illustrates this quasi-isentropic part of their experiments, where the isentropes from the EOS models are calculated to pass through

the temperatures and densities reported by Zheng *et al.* for the third shock state in each of their six shots. These shock states are represented by the leftmost points in the figure; the first and second shock states are not plotted since the figure focuses on just quasi-isentropic compression. S5764 [21] agrees fairly well with the experimental data on the pressure, but its predicted temperatures tend to be too high. On the other hand, the Chabrier *et al.* EOS [10] falls within the error bars of most of the experimentally reported temperature points, but its predicted pressures tend to be too low. L21 falls somewhere in between the two opposite extremes represented by these two other EOS models. The pressures from L21 agree fairly well with the Zheng *et al.* [91] data, and while its predicted temperatures for most of the points are too high like in the case of S5764, they are significantly lower and closer to the experimental data.

Finally, we conclude the discussion of our results with Fig. 12, which compares high-temperature isotherms from L21 and S5764 [21] with predictions from two theoretical

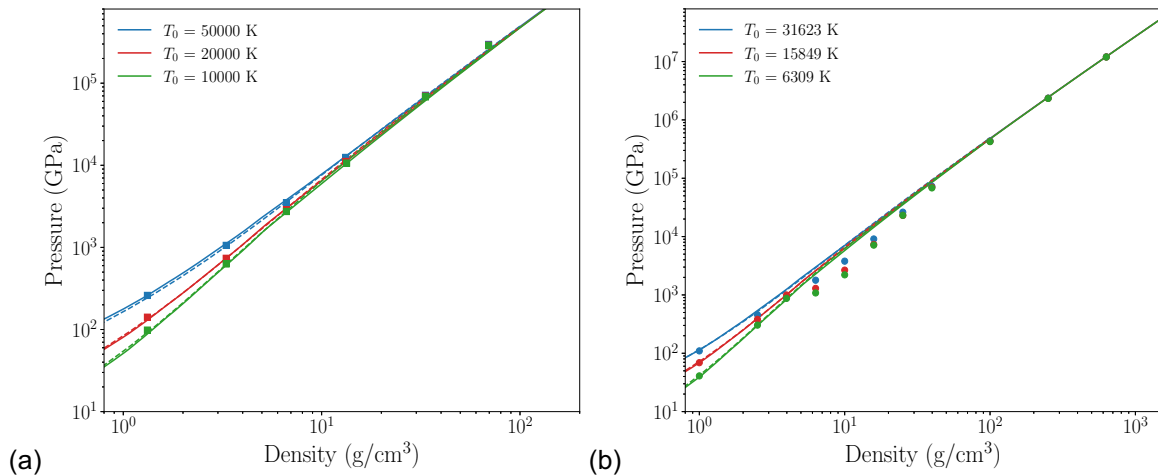


FIG. 12. High-temperature isotherms from L21 (solid curves) and S5764 [21] (dashed curves) compared against theoretical predictions, where (a) compares Stixrude and Jeanloz [92] (squares) with the EOS models, and (b) compares Winisdoerffer and Chabrier [93] (circles) with the EOS models.

studies: 1) Stixrude and Jeanloz [92] and 2) Winisdoerffer and Chabrier [93]. For clarity, we do not show results from the Chabrier *et al.* EOS [10] in the figure, but we find that it yields similar results as L21 and S5764. Stixrude and Jeanloz perform *ab initio* QMD simulations, while Winisdoerffer and Chabrier employ a “chemical model” [8,94,95] that minimizes a free-energy function to determine the composition of neutral He,  $\text{He}^+$ ,  $\text{He}^{++}$ , and electrons  $e^-$  as a function of temperature and density. The EOS models agree with both sets of theoretical simulations [92,93] at the low-density end, and they also agree with the high-density end in Winisdoerffer and Chabrier, confirming that all of the results in the figure approach the one-component plasma limit. It is at intermediate densities from about 10–100  $\text{g}/\text{cm}^3$  where differences can be seen. In this density range, the EOS models predict pressures that are higher than those from Winisdoerffer and Chabrier, but lower than those from Stixrude and Jeanloz, though they appear to be closer to the pressures from the latter study, especially at densities near 10  $\text{g}/\text{cm}^3$ . This seems to imply that the chemical model from Winisdoerffer and Chabrier underpredicts the extent of ionization in this intermediate density range, though no experimental studies are available in this range to validate this hypothesis. The only available set of results that provide any overlap with this 10–100  $\text{g}/\text{cm}^3$  density range are the quasi-isentropic data (derived through a combination of experimental measurements and hydrodynamic/EOS models) from Mochalov *et al.* [83–88] illustrated in Fig. 10, which extend up to about 10  $\text{g}/\text{cm}^3$  and show good agreement with the EOS models.

#### IV. CONCLUSIONS

We have performed experiments in which liquid He at cryogenic temperatures is shock compressed to a peak pressure of 125 GPa. These experiments probe conditions that have not been accessed in previous experiments. We have also performed *ab initio* QMD simulations, with nuclear quantum corrections for the zero-point energy and pressure, that are consistent with our shock measurements. Our results

demonstrate that for He, the quantum effects are negligible at our initial conditions. Comparisons of the available EOS models with our experiments and QMD simulations motivated the development of our own He EOS, which we refer to as L21. This EOS covers temperatures and pressures relevant to multiple different fluid states, ranging from gases, to compressed liquids, to high-temperature shocked plasmas. It is not intended, however, to give an accurate representation of the vapor–liquid dome or the critical point; an improved treatment of that region will be reserved for a future study. By design, L21 gives good agreement with our experimental and QMD results. We have demonstrated that L21 also yields good overall agreement with the published static-compression data and other shock-compression data on He.

Although the aforementioned studies have collectively done an excellent job in furthering our understanding of He, much of the relevant phase space has still not been explored. Further experimental work would help provide additional constraints on the thermodynamic behavior of He at extreme conditions. Moreover, we note that a highly accurate, multiphase He EOS that covers a wide range of conditions, including those pertaining to the hcp and fcc solid phases, has still not been developed. The closest such EOS model currently available in this regard may be S5764 developed by Kerley [21], which is a two-phase EOS that covers fluid (including the various incarnations like gases, ordinary liquids, and ionized plasmas) and hcp, but not the fcc phase. A necessary step in developing an accurate multiphase EOS for He is to construct a fluid-phase EOS that can describe both the vapor-liquid dome and high-temperature plasma states to a high degree of fidelity, as well as all states in between these two extremes. This could perhaps be achieved by patching L21 to one of the published multiparameter fluid EOS models [1,11–14], the latter of which provides a highly parametrized fit to the vapor-liquid dome, critical point, and other low-temperature, low-pressure regimes. The resulting fluid-phase model could then be combined with separate models for hcp and fcc to construct the multiphase EOS.

## ACKNOWLEDGMENTS

This work was performed under the auspices of the U.S. Department of Energy (DOE) by Lawrence Livermore National Laboratory under Contract No. DE-AC52-07NA27344. We thank the operations team at Sandia's Z-machine and the Z target fabrication team for conducting the experiments and the target metrology. We thank Joe Hanson, Keegan Shelton, Jose Villalva, and Adam York for assembling the helium targets, the helium cryostat, and running the cryogenics system. Their hard work is what makes these experiments possible. We also thank Michael Wadas and Marius Millot for helpful discussions on the data pertaining to Fig. 9. Sandia National Laboratories is a multimission laboratory managed and operated by National Technology & Engineering Solutions of Sandia, LLC, a wholly owned subsidiary of Honeywell International Inc., for the U.S. Department of Energy's National Nuclear Security Administration under Contract No. DE-NA0003525. This paper describes objective technical results and analysis. Any subjective views or opinions that might be expressed in the paper do not necessarily represent the views of the U.S. Department of Energy or the United States Government.

## APPENDIX: EOS MODEL SUMMARY

The EOS in its most fundamental form is given by Eq. (2), which reads  $F(T, \rho) = F_{\text{cold}}(\rho) + F_{\text{ion}}(T, \rho) + F_{\text{electron}}(T, \rho)$ . The electron-thermal term  $F_{\text{electron}}(T, \rho)$  is fixed by virtue of our choice to model this term with PURGATORIO, which does not involve any adjustable parameters and is an all-electron, relativistic DFT-based atom-in-jellium model developed by Wilson, Sterne, and others [71,72]. The cold curve  $F_{\text{cold}}(\rho)$  is experimentally constrained over the range from about 0.1–1 g/cm<sup>3</sup> through the room-temperature isotherm data illustrated in Fig. 4. Although the ion-thermal term  $F_{\text{ion}}(T, \rho)$  makes a non-negligible contribution along this isotherm [as shown in Fig. 4(c)], the isotherm is nevertheless largely a reflection of  $F_{\text{cold}}(\rho)$ , and so the data provide a powerful constraint on  $P_{\text{cold}}(\rho) = -\rho^2 dF_{\text{cold}}(\rho)/d\rho$ , from which we can obtain  $F_{\text{cold}}(\rho)$  by integration. Below 0.1 g/cm<sup>3</sup>, we utilize splines to join  $F_{\text{cold}}(\rho)$  to a soft-sphere model [28,63,64], although we have noted that an improved treatment of the critical region could be achieved in the future by replacing this low-density region of the EOS with one of the multiparameter EOS models [1,11–14] that are specialized for lower densities and temperatures. At extreme compressions (say, densities above 50 g/cm<sup>3</sup>), we assume that PURGATORIO provides an accurate description of the cold curve, as explained in Sec. II C and our earlier publications [28–30]. We again use splines to connect  $F_{\text{cold}}(\rho)$  in the experimentally constrained 0.1–1 g/cm<sup>3</sup> range to the PURGATORIO calculations that reside at much higher densities.

TABLE IV. Polynomial fits over the range from 0.1–3 g/cm<sup>3</sup> for the cold energy  $F_{\text{cold}}(\rho) = \sum_{k=0}^3 c_k \rho^k$  in units of kJ/mol and Debye temperature  $\theta(\rho) = \sum_{k=0}^4 c_k \rho^k$  in units of K, with the coefficients  $c_k$  listed here.

Property	$c_0$	$c_1$	$c_2$	$c_3$	$c_4$
$F_{\text{cold}}$	5.295	-32.152	50.313	-4.544	
$\theta$	-5.032	109.002	-38.068	15.152	-2.112

The ion-thermal free energy  $F_{\text{ion}}(T, \rho)$  is represented with the Cowan model in Eq. (3). This model is described by two parameters:  $\alpha$  and  $\theta = \theta(\rho)$ . As an alternative to working directly with the Debye temperature  $\theta(\rho)$ , one could instead integrate the ion-thermal Grüneisen parameter  $\gamma_{\text{ion}}(\rho) = d \ln \theta(\rho)/d \ln \rho$  and set the integration constant by specifying a value for the Debye temperature  $\theta_{\text{ref}} = \theta(\rho_{\text{ref}})$  at an arbitrarily chosen reference density  $\rho_{\text{ref}}$ . For the purposes of EOS construction, it is generally easier to work with  $\gamma_{\text{ion}}(\rho)$  rather than  $\theta(\rho)$  because adjustments to  $\gamma_{\text{ion}}$  have more of a visible effect on the pressure  $P = P(T, \rho)$  returned by the EOS, and the majority of data available to constrain the EOS pertain to the pressure. The room-temperature isotherm data in Fig. 4, together with the shock- and ramp-compression data discussed in Secs. III B and III C, provide constraints on  $\gamma_{\text{ion}}(\rho)$  over a density range from about 0.001–20 g/cm<sup>3</sup>. Below this density range, we employ splines to extrapolate  $\gamma_{\text{ion}}$  to the ideal-gas (zero-density) limit of  $\gamma_{\text{ion}} = 2/3$ , and above this density range, we extrapolate  $\gamma_{\text{ion}}$  to the one-component plasma limit [29,96] of  $\gamma_{\text{ion}} = 1/2$ . The two free-energy terms  $F_{\text{cold}}(\rho)$  and  $F_{\text{ion}}(T, \rho)$  are coupled since they both make non-negligible contributions to the room-temperature isotherm, and so  $\gamma_{\text{ion}}(\rho)$  is adjusted together with  $F_{\text{cold}}(\rho)$  through the iterative procedure described near the end of Sec. III A. There is some degeneracy between the parameter  $\alpha$  and the reference Debye temperature  $\theta_{\text{ref}}$  in that both provide a constant offset and a  $T, \rho$ -independent scaling on the free energy, as can be seen from Equation (3). If we were developing a multiphase EOS, more constraints (e.g., melt curves) may be available to break this degeneracy. However, for the fluid-phase-only EOS that we construct in the present study, we have chosen to arbitrarily set  $\alpha$  to a value of 100 g<sup>2/3</sup>/(K · cm<sup>2</sup>), and adjust  $\theta_{\text{ref}}$  to reproduce the entropy results in Fig. 5, leading to  $\theta_{\text{ref}} = 11.5$  K at  $\rho_{\text{ref}} = 0.1624$  g/cm<sup>3</sup>.

The EOS is stored in tabular form over a grid of points in temperature-density space. For this paper, we have used a 3000×600 grid, with the 3000 temperature (600 density) points spaced logarithmically from 1 K to 10<sup>9</sup> K (10<sup>-10</sup> to 5000 g/cm<sup>3</sup>). An electronic copy of this table may be available for distribution upon reasonable request. The broad range of conditions spanned by the EOS, along with the use of PURGATORIO, preclude the possibility of representing the EOS over the entire range with a single analytical model, but Table IV presents polynomial fits for  $F_{\text{cold}}(\rho)$  and  $\theta(\rho)$  over the limited range 0.1–3 g/cm<sup>3</sup>.

[1] D. O. Ortiz Vega, A New Wide Range Equation of State for Helium-4, Ph.D. thesis, Texas A&M University (2013).

[2] S. E. Donnelly, The density and pressure of helium in bubbles in implanted metals: A critical review, *Rad. Effects* **90**, 1 (1985).

- [3] W. G. Wolfer, Radiation effects in plutonium: What is known? Where should we go from here? Los Alamos Science, No. 26 LA-UR-00-4100-32 (Los Alamos National Laboratory, 2000).
- [4] R. B. Schwarz, D. E. Hooks, J. J. Dick, J. I. Archuleta, and A. R. Martinez, Resonant ultrasound spectroscopy measurement of the elastic constants of cyclotrimethylene trinitramine, *J. Appl. Phys.* **98**, 056106 (2005).
- [5] B. W. Chung, S. R. Thompson, K. E. Lema, D. S. Hiromoto, and B. B. Ebbinghaus, Evolving density and static mechanical properties in plutonium from self-irradiation, *J. Nucl. Mater.* **385**, 91 (2009).
- [6] B. W. Chung, K. E. Lema, and P. G. Allen, Effects of self-irradiation in plutonium alloys, *J. Nucl. Mater.* **471**, 239 (2016).
- [7] J. R. Jeffries, J. A. Hammons, T. M. Willey, M. A. Wall, D. Ruddle, J. Ilavsky, P. G. Allen, and T. van Buuren, Probing He bubbles in naturally aged and annealed  $\delta$ -Pu alloys using ultra-small-angle x-ray scattering, *J. Nucl. Mater.* **498**, 505 (2018).
- [8] D. Saumon, G. Chabrier, and H. M. van Horn, An equation of state for low-mass stars and giant planets, *Astrophys. J. Suppl. Ser.* **99**, 713 (1995).
- [9] A. Becker, W. Lorenzen, J. J. Fortney, N. Nettelmann, M. Schöttler, and R. Redmer, Ab initio equations for hydrogen (H-REOS.3) and helium (He-REOS.3) and their implications for the interior of brown dwarfs, *Astrophys. J. Suppl. Ser.* **215**, 21 (2014).
- [10] G. Chabrier, S. Mazevet, and F. Soubiran, A new equation of state for dense hydrogen–helium mixtures, *Astrophys. J.* **872**, 51 (2019).
- [11] R. D. McCarty, Thermodynamic properties of helium 4 from 2 to 1500 K at pressures to  $10^8$  Pa, *J. Phys. Chem. Ref. Data* **2**, 923 (1973).
- [12] R. D. McCarty and V. D. Arp, *A New Wide Range Equation of State for Helium* (Springer, Boston, 1990), Vol. 35, pp. 1465–1475.
- [13] S. Kaviani, F. Feyzi, and B. Khosravi, Modification of the Peng–Robinson equation of state for helium in low temperature regions, *Phys. Chem. Liq.* **54**, 542 (2016).
- [14] J. W. Leachman, R. T. Jacobsen, E. W. Lemmon, and S. G. Penoncello, in *Thermodynamic Properties of Cryogenic Fluids*, edited by S. W. Van Scriver and S. Jeong, International Cryogenics Monograph Series (Springer International Publishing AG, Cham, 2017).
- [15] J. Lindl, Development of the indirect-drive approach to inertial confinement fusion and the target physics basis for ignition and gain, *Phys. Plasmas* **2**, 3933 (1995).
- [16] H. Abu-Shawareb, R. Acree, P. Adams, J. Adams, B. Addis, R. Aden, P. Adrian, B. Afeyan, M. Aggleton, L. Aghaian, A. Aguirre *et al.*, Lawson criterion for ignition exceeded in an inertial fusion experiment, *Phys. Rev. Lett.* **129**, 075001 (2022).
- [17] D. B. Sinars, M. A. Sweeney, C. S. Alexander *et al.*, Review of pulsed power-driven high energy density physics research on Z at sandia, *Phys. Plasmas* **27**, 070501 (2020).
- [18] D. A. Young, A. K. McMahan, and M. Ross, Equation of state and melting curve of helium to very high pressure, *Phys. Rev. B* **24**, 5119 (1981).
- [19] M. Ross and D. A. Young, Helium at high density, *Phys. Lett. A* **118**, 463 (1986).
- [20] D. A. Young, *Phase Diagrams of the Elements* (University of California Press, Berkeley and Los Angeles, 1991).
- [21] G. I. Kerley, An equation of state for helium, Technical report KTS04-2 (Kerley Technical Services, 2004).
- [22] M. Lallemand and D. Vidal, Variation of the polarizability of noble gases with density, *J. Chem. Phys.* **66**, 4776 (1977).
- [23] A. Polian and M. Grimsditch, Elastic properties and density of helium up to 20 GPa, *Europhys. Lett.* **2**, 849 (1986).
- [24] P. J. Kortbeek, J. J. van de Ridder, S. N. Biswas, and J. A. Schouten, Measurement of the compressibility and sound velocity of helium up to 1 GPa, *Int. J. Thermophys.* **9**, 425 (1988).
- [25] R. Le Toullec, P. Loubeyre, and J. P. Pinceaux, Refractive-index measurements of dense helium up to 16 GPa at  $T = 298$  K: Analysis of its thermodynamic and electronic properties, *Phys. Rev. B* **40**, 2368 (1989).
- [26] A. Dewaele, J. H. Eggert, P. Loubeyre, and R. LeToullec, Measurement of refractive index and equation of state in dense He,  $H_2$ ,  $H_2O$ , and Ne under high pressure in a diamond anvil cell, *Phys. Rev. B* **67**, 094112 (2003).
- [27] W. J. Nellis, N. C. Holmes, A. C. Mitchell, R. J. Trainor, G. K. Governo, M. Ross, and D. A. Young, Shock compression of liquid helium to 56 GPa (560 kbar), *Phys. Rev. Lett.* **53**, 1248 (1984).
- [28] C. J. Wu, D. A. Young, P. A. Sterne, and P. C. Myint, Equation of state for a chemically dissociative, polyatomic system: Carbon dioxide, *J. Chem. Phys.* **151**, 224505 (2019).
- [29] C. J. Wu, P. C. Myint, J. E. Pask, C. J. Prisbrey, A. A. Correa, P. Suryanarayana, and J. B. Varley, Development of a multiphase beryllium equation of state and physics-based variations, *J. Phys. Chem. A* **125**, 1610 (2021).
- [30] C. J. Wu, L. X. Benedict, P. C. Myint, S. Hamel, C. J. Prisbrey, and J. R. Leek, Wide-ranged multiphase equation of state for iron and model variations addressing uncertainties in high-pressure melting, *Phys. Rev. B* **108**, 014102 (2023).
- [31] M. K. Matzen, Z pinches as intense X-ray sources for high-energy density physics applications, *Phys. Plasmas* **4**, 1519 (1997).
- [32] M. Savage, L. Bennett, D. Bliss, W. Clark, R. Coats, J. Elizondo, K. LeChien, H. Harjes, J. Lehr, J. Maenchen, D. McDaniel *et al.*, An overview of pulse compression and power flow in the upgraded Z pulsed power driver, in *Proceedings of the 2007 IEEE Pulsed Power Conference* (IEEE, New York, 2007), Vol. 1–4, p. 979.
- [33] R. W. Lemke, M. D. Knudson, C. A. Hall, T. A. Hail, M. P. Desjarlais, J. R. Asay, and T. A. Mehlhorn, Characterization of magnetically accelerated flyer plates, *Phys. Plasmas* **10**, 1092 (2003).
- [34] R. W. Lemke, M. D. Knudson, D. E. Bliss, K. Cochrane, J.-P. Davis, A. A. Giunta, H. C. Harjes, and S. A. Slutz, Magnetically accelerated, ultrahigh velocity flyer plates for shock wave experiments, *J. Appl. Phys.* **98**, 073530 (2005).
- [35] R. W. Lemke, M. D. Knudson, and J.-P. Davis, Magnetically driven hyper-velocity launch capability at the Sandia Z-Accelerator, *Int. J. Impact Engng.* **38**, 480 (2011).
- [36] M. D. Knudson, R. W. Lemke, D. B. Hayes, C. A. Hall, C. Deeney, and J. R. Asay, Near-absolute hughoniot measurements in aluminum to 500 GPa using a magnetically accelerated flyer plate technique, *J. Appl. Phys.* **94**, 4420 (2003).
- [37] M. D. Knudson, D. L. Hanson, J. E. Bailey, C. A. Hall, J. R. Asay, and C. Deeney, Principal hughoniot, reverberating wave, and mechanical reshock measurements of liquid deuterium to

- 400 GPa using plate impact techniques, *Phys. Rev. B* **69**, 144209 (2004).
- [38] M. D. Knudson and M. P. Desjarlais, Shock compression of quartz to 1.6 TPa: Redefining a pressure standard, *Phys. Rev. Lett.* **103**, 225501 (2009).
- [39] S. Root, R. J. Magyar, J. H. Carpenter, D. L. Hanson, and T. R. Mattsson, Shock compression of a fifth period element: Liquid xenon to 840 GPa, *Phys. Rev. Lett.* **105**, 085501 (2010).
- [40] T. R. Mattsson, S. Root, A. E. Mattsson, L. Shulenburg, R. J. Magyar, and D. G. Flicker, Validating density functional theory simulations at high energy-density conditions with liquid krypton shock experiments to 850 GPa on sandia's Z-machine, *Phys. Rev. B* **90**, 184105 (2014).
- [41] S. Root, C. A. McCoy, K. R. Cochrane, J. H. Carpenter, R. W. Lemke, L. Shulenburg, T. R. Mattsson, and P. A. Sterne, Argon equation of state data to 1 TPa: Shock compression experiments and simulations, *Phys. Rev. B* **106**, 174114 (2022).
- [42] D. L. Hanson, A. J. Lopez, M. D. Knudson, S. Root, M. E. Cuneo, J. R. Asay, K. P. Shelton, J. M. Villalva, and D. G. Schroen, Cryogenic targets for dynamic material properties and fusion studies at sandia national laboratories, Tech. Rep. SAND2011-7027C (Sandia National Laboratories, 2011).
- [43] E. C. Kerr, Density of liquid He<sup>4</sup>, *J. Chem. Phys.* **26**, 511 (1957).
- [44] L. M. Barker and R. E. Hollenbach, Laser interferometer for measuring high velocities of any reflecting surface, *J. Appl. Phys.* **43**, 4669 (1972).
- [45] M. H. Edwards, The index of refraction of liquid helium, *Can. J. Phys.* **34**, 898 (1956).
- [46] B. Militzer, First principles calculations of shock compressed fluid helium, *Phys. Rev. Lett.* **97**, 175501 (2006).
- [47] S. Root, K. R. Cochrane, J. H. Carpenter, and T. R. Mattsson, Carbon dioxide shock and reshock equation of state data to 8 Mbar: Experiments and simulations, *Phys. Rev. B* **87**, 224102 (2013).
- [48] M. D. Knudson and M. P. Desjarlais, Adiabatic release measurements in  $\alpha$ -quartz between 300 and 1200 GPa: Characterization of  $\alpha$ -quartz as a shock standard in the multi-megabar regime, *Phys. Rev. B* **88**, 184107 (2013).
- [49] M. P. Desjarlais, M. D. Knudson, and K. R. Cochrane, Extension of the hugoniot and analytical release model of  $\alpha$ -quartz to 0.2-3 TPa, *J. Appl. Phys.* **122**, 035903 (2017).
- [50] M. D. Knudson and M. P. Desjarlais, High-precision shock wave measurements of deuterium: Evaluation of exchange-correlation functionals at the molecular-to-atomic transition, *Phys. Rev. Lett.* **118**, 035501 (2017).
- [51] P. Hohenberg and W. Kohn, Inhomogeneous electron gas, *Phys. Rev.* **136**, B864 (1964).
- [52] W. Kohn and L. J. Sham, Self-consistent equations including exchange and correlation effects, *Phys. Rev.* **140**, A1133 (1965).
- [53] M. D. Knudson, M. P. Desjarlais, and D. H. Dolan, Shock-wave exploration of the high-pressure phases of carbon, *Science* **322**, 1822 (2008).
- [54] S. Root, J. P. Townsend, E. Davies, R. W. Lemke, D. E. Bliss, D. E. Fratanduono, R. G. Kraus, M. Millot, D. K. Spaulding, L. Shulenburg, S. T. Stewart, and S. B. Jacobsen, The principal hugoniot of forsterite to 950 GPa, *Geophys. Res. Lett.* **45**, 3865 (2018).
- [55] N. D. Mermin, Thermal properties of the inhomogeneous electron gas, *Phys. Rev.* **137**, A1441 (1965).
- [56] J. P. Perdew, K. Burke, and M. Ernzerhof, Generalized gradient approximation made simple, *Phys. Rev. Lett.* **77**, 3865 (1996).
- [57] G. Kresse and J. Hafner, *Ab initio* molecular dynamics for liquid metals, *Phys. Rev. B* **47**, 558 (1993).
- [58] G. Kresse and J. Furthmüller, Efficient iterative schemes for *ab initio* total-energy calculations using a plane-wave basis set, *Phys. Rev. B* **54**, 11169 (1996).
- [59] A. E. Mattsson, P. A. Schultz, M. P. Desjarlais, T. R. Mattsson, and K. Leung, Designing meaningful density functional theory calculations in materials science—a primer, *Modell. Simul. Mater. Sci. Eng.* **13**, R1 (2005).
- [60] F. H. Ree, Simple mixing rule for mixtures with exp-6 interactions, *J. Chem. Phys.* **78**, 409 (1983).
- [61] V. Kapil, M. Rossi, O. Marsalek, R. Petraglia, Y. Litman, T. Spura, B. Cheng, A. Cuzzocrea, R. H. Meißner, D. M. Wilkins, B. A. Helfrecht, P. Juda, S. P. Bienvenue, W. Fang, J. Kessler, I. Poltavsky, S. Vandenbrande, J. Wieme, C. Corminboeuf, T. D. Kühne *et al.*, i-PI 2.0: A universal force engine for advanced molecular simulations, *Comput. Phys. Commun.* **236**, 214 (2019).
- [62] A. P. Thompson, H. M. Aktulga, R. Berger, D. S. Bolintineanu, W. M. Brown, P. S. Crozier, P. J. in 't Veld, A. Kohlmeyer, S. G. Moore, T. D. Nguyen, R. Shan, M. J. Stevens, J. Tranchida, C. Trott, and S. J. Plimpton, LAMMPS - a flexible simulation tool for particle-based materials modeling at the atomic, meso, and continuum scales, *Comput. Phys. Commun.* **271**, 108171 (2022).
- [63] R. M. More, K. H. Warren, D. A. Young, and G. B. Zimmerman, A new quotidian equation of state (QEOS) for hot dense matter, *Phys. Fluids* **31**, 3059 (1988).
- [64] D. A. Young and E. M. Corey, A new global equation of state model for hot, dense matter, *J. Appl. Phys.* **78**, 3748 (1995).
- [65] E. D. Chisolm and D. C. Wallace, Dynamics of monatomic liquids, *J. Phys.: Condens. Matter* **13**, R739 (2001).
- [66] D. C. Wallace, *Statistical Physics of Crystals and Liquids: A Guide to Highly Accurate Equations of State* (World Scientific Publishing Company, Singapore, 2002), p. 328.
- [67] E. C. Chisolm, S. D. Crockett, and D. C. Wallace, Test of a theoretical equation of state for elemental solids and liquids, *Phys. Rev. B* **68**, 104103 (2003).
- [68] S. D. Crockett and C. W. Greeff, A gallium multiphase equation of state, *AIP Conf. Proc.* **1195**, 1191 (2009).
- [69] F. N. Fritsch, The LEOS interpolation package, Technical Report UCRL-ID-148554-REV-1 (Lawrence Livermore National Laboratory, 2003), p. 30.
- [70] R. L. Mills, D. H. Liebenberg, and J. C. Bronson, Equation of state and melting properties of <sup>4</sup>He from measurements to 20 kbar, *Phys. Rev. B* **21**, 5137 (1980).
- [71] B. Wilson, V. Sonnad, P. Sterne, and W. Isaacs, PURGATORIO—a new implementation of the Inferno algorithm, *J. Quant. Spectrosc. Radiat. Transfer* **99**, 658 (2006).
- [72] P. A. Sterne, S. B. Hansen, B. G. Wilson, and W. A. Isaacs, Equation of state, occupation probabilities and conductivities in the average atom PURGATORIO code, *High Energ. Density Phys.* **3**, 278 (2007).
- [73] J. T. Larsen, *Foundations of High-Energy-Density Physics: Physical Processes of Matter at Extreme Conditions* (Cambridge University Press, Cambridge, 2017).

- [74] A. A. Correa, L. X. Benedict, M. A. Morales, P. A. Sterne, J. I. Castor, and E. Schwegler, A first-principles global multiphase equation of state for hydrogen, [arXiv:1806.01346v1](https://arxiv.org/abs/1806.01346v1).
- [75] C. W. Cranfill and R. M. More, IONEOS: A fast, analytic, ion equation-of-state routine, Technical Report LA-7313-MS (Los Alamos Scientific Laboratory, 1978).
- [76] C. T. Seagle, R. W. D., A. J. Lopez, R. J. Hickman, and T. F. Thornhill III, High precision Hugoniot measurements on statically pre-compressed fluid helium, *J. Appl. Phys.* **120**, 125902 (2016).
- [77] L. Cai, Q. Chen, Y. Gu, Y. Zhang, X. Zhou, and F. Jing, Equation of state of fluid helium at high temperatures and densities, *Sci. Chin. Ser. G* **48**, 695 (2005).
- [78] S. Brygoo, M. Millot, P. Loubeyre, A. E. Lazicki, S. Hamel, T. Qi, P. M. Celliers, F. Coppari, J. H. Eggert, D. E. Fratanduono, D. G. Hicks, J. R. Ryan, R. F. Smith, D. C. Swift, G. W. Colins, and R. Jeanloz, Analysis of laser shock experiments on pre-compressed samples using a quartz reference and application to warm dense hydrogen and helium, *J. Appl. Phys.* **118**, 195901 (2015).
- [79] J. Eggert, S. Brygoo, P. Loubeyre, R. S. McWilliams, P. M. Celliers, D. G. Hicks, T. R. Boehly, R. Jeanloz, and G. W. Collins, Hugoniot data for helium in the ionization regime, *Phys. Rev. Lett.* **100**, 124503 (2008).
- [80] P. M. Celliers, P. Loubeyre, J. H. Eggert, S. Brygoo, R. S. McWilliams, D. G. Hicks, T. R. Boehly, R. Jeanloz, and G. W. Collins, Insulator-to-conducting transition in dense fluid helium, *Phys. Rev. Lett.* **104**, 184503 (2010).
- [81] B. Militzer, Path integral Monte Carlo and density functional molecular dynamics simulations of hot, dense helium, *Phys. Rev. B* **79**, 155105 (2009).
- [82] M. Preising, W. Lorenzen, A. Becker, R. Redmer, M. D. Knudson, and M. P. Desjarlais, Equation of state and optical properties of warm dense helium, *Phys. Plasmas* **25**, 012706 (2018).
- [83] M. A. Mochalov, R. I. Il'kaev, V. E. Fortov, A. L. Mikhailov, V. A. Arinin, A. O. Blikov, A. Y. Baurin, V. A. Komrakov, V. A. Ogorodnikov, A. V. Ryzhkov, A. A. Yukhimchuk, Measurement of the quasi-isentropic compressibility of a helium plasma at a pressure of about 5000 GPa, *JETP Lett.* **96**, 158 (2012).
- [84] M. A. Mochalov, R. I. Il'kaev, V. E. Fortov, A. L. Mikhailov, Y. M. Makarov, V. A. Arinin, A. O. Blikov, A. Y. Baurin, V. A. Komrakov, V. A. Ogorodnikov, A. V. Ryzhkov, E. A. Pronin, and A. A. Yukhimchuk, Measurement of quasi-isentropic compressibility of helium and deuterium at pressures of 1500–2000 GPa, *J. Exp. Theor. Phys.* **115**, 614 (2012).
- [85] M. A. Mochalov, R. I. Il'kaev, V. E. Fortov, A. L. Mikhailov, V. A. Arinin, A. O. Blikov, V. A. Komrakov, A. V. Ryzhkov, V. A. Ogorodnikov, and A. A. Yukhimchuk, Thermodynamic properties of a nonideal helium plasma at quasi-isentropic compression by a factor of 575 at a pressure of 3000 GPa, *JETP Lett.* **101**, 519 (2015).
- [86] M. A. Mochalov, R. I. Il'kaev, V. E. Fortov, A. L. Mikhailov, V. A. Arinin, A. O. Blikov, S. E. Elfimov, V. A. Komrakov, V. A. Ogorodnikov, and A. V. Ryzhkov, Thermodynamic parameters of helium under shock-wave and quasi-isentropic compressions at pressures up to 4800 GPa and compression ratios up to 90, *J. Exp. Theor. Phys.* **125**, 948 (2017).
- [87] M. A. Mochalov, R. I. Il'kaev, V. E. Fortov, A. L. Mikhailov, V. A. Arinin, A. O. Blikov, V. A. Ogorodnikov, A. V. Ryzhkov, V. A. Komrakov, and I. P. Maksimkin, Measurement of quasi-isentropic compressibility of gaseous helium at a pressure of  $\sim 10$  TPa, *JETP Lett.* **108**, 656 (2018).
- [88] M. A. Mochalov, R. I. Il'kaev, V. E. Fortov, S. V. Erunov, V. A. Arinin, A. O. Blikov, V. A. Komrakov, I. P. Maksimkin, V. A. Ogorodnikov, A. V. Ryzhkov, V. K. Gryaznov, I. L. Iosilevskiy, P. R. Levashov, Y. S. Lavrinenko, I. V. Morozov, D. V. Minakov, M. A. Paramonov, and A. V. Shutov, Compressibility of non-ideal deuterium and helium plasmas up to 20 TPa, *J. Exp. Theor. Phys.* **133**, 630 (2021).
- [89] M. Zhernokletov, V. A. Arinin, V. N. Buzin, Y. A. Grigorieva, N. B. Davydov, and V. V. Khrustalev, Quasi-isentropic compression of gaseous helium in pressure range from 130 to 460 GPa, *AIP Conf. Proc.* **1426**, 1411 (2012).
- [90] M. V. Zhernokletov, V. K. Gryaznov, V. A. Arinin, V. N. Buzin, N. B. Davydov, R. I. Il'kaev, I. L. Iosilevskiy, A. L. Mikhailov, M. G. Novikov, V. V. Khrustalev, and V. E. Fortov, Quasi-isentropic compression of dense gaseous helium at pressures up to 500 GPa, *JETP Lett.* **96**, 432 (2012).
- [91] J. Zheng, Q. F. Chen, Y. J. Gu, J. T. Li, Z. G. Li, C. J. Li, and Z. Y. Chen, Shock-adiabatic to quasi-isentropic compression of warm dense helium up to 150 GPa, *Phys. Rev. B* **95**, 224104 (2017).
- [92] L. Stixrude and R. Jeanloz, Fluid helium at conditions of giant planetary interiors, *Proc. Natl. Acad. Sci.* **105**, 11071 (2008).
- [93] C. Winisdoerffer and G. Chabrier, Free-energy model for fluid helium at high density, *Phys. Rev. E* **71**, 026402 (2005).
- [94] A. Förster, T. Kahlbaum, and W. Ebeling, Equation of state and the phase diagram of dense fluid helium in the region of partial ionization, *Laser Part. Beams* **10**, 253 (1992).
- [95] J. M. Aparicio and G. Chabrier, Free-energy model for fluid atomic helium at high density, *Phys. Rev. E* **50**, 4948 (1994).
- [96] S. Eliezer, A. Ghatak, and H. Hora, *Fundamentals of Equations of State* (World Scientific Publishing Company, Singapore, 2002).